ISSN: 0976 – 2965
IJBET (2017), 6(4):32-37

Impact of cloudiness on longwave radiation exchange at exterior greenhouse surfaces

Erick Kiplangat Ronoh
Agricultural and Biosystems Engineering Department, Jomo Kenyatta University of Agriculture and Technology, P.O. Box 62000-00200, Nairobi, Kenya
ronoh@jkuat.ac.ke

ABSTRACT:
Cloudiness influences the weather on earth and especially the longwave radiation received by exterior surfaces of buildings such as greenhouses. Precise estimation of cloudiness is therefore vitally important for numerous applications in agriculture requiring surface radiation and energy balance. This study aims at estimating cloudiness factors using two approaches (octas and weather maps) and testing their usage in longwave radiation simulation at an experimental greenhouse surface. With this information, the problem of missing cloudiness data at any given time and in any location can be solved. From this study, the results indicate that better model predictions of longwave radiation were obtained by simulation with weather maps than with octas. Hence, map-based simulation data are accurate and precise enough for this kind of energy application. Despite the slight variations, the usage of cloudiness factors showed insignificant differences in terms of radiation simulation. Overall, the generated cloudiness information could be used in various agricultural modelling applications.

Keywords: cloudiness; longwave radiation exchange; exterior surface; greenhouse; agriculture; energy

INTRODUCTION

In the past, numerous attempts have been made to quantify cloud cover necessary in weather prediction models. The improvements of analyses and forecasts is small, yet the authors consider the procedure promising [1, 2]. Cloudiness influences the longwave radiation emitted by the atmosphere downward to the earth's surface. Although the radiative fluxes can be calculated with reasonable accuracy using complex radiation models, detailed measurements of the air column above any measurement site (including cloudiness, temperature, water vapour, trace gases and aerosols) are required [3]. Due to a void of such atmospheric parameters, especially cloudiness [4], longwave radiative fluxes have received less attention than shortwave fluxes.

Clouds are known to alter both the shortwave and longwave radiative profiles. This is through both scattering and absorption of incident solar radiation as well as emission of longwave radiation from cloud base [5]. Therefore, accurate prediction of this cloudiness is necessary to allow proper representation in globate climate simulations in different agricultural and horticultural applications. Hence, the objective of this study is to estimate the cloudiness factor during both day and night and test its appropriateness in longwave radiation exchange at an exterior greenhouse surface. Such an exterior surface is shown in Figure 1, which is typical of greenhouse glass-covered surfaces.

MATERIALS AND METHODS

1. Cloudiness prediction and radiation

The cloudiness factor is a very important parameter in the longwave radiation exchange. This was established using two approaches (Table 1). The first approach involved acquisition of octas (eighths) given by German Weather Service (Deutscher Wetterdienst) [6], while the second method was through computer-based analysis of weather maps from the web-service *Weather Online* (WetterOnline) [7]. Estimation of cloudiness in form of octas relied on only one recorded value per hour which is assigned through visual inspection of the sky by experienced weather watchers. Basically, the octas express the number of eighths of the sky that is cloud-covered. For the vision-based approach, about 12 weather maps per hour (interval of 5 minutes) were analyzed and an hourly mean obtained. For both daytime and nighttime situations, hourly means were computed and used in the analysis.

The weather maps provide sufficient weather elements over a geographical area at a specified time. A computer vision-based algorithm was developed in Halcon 11.0 and it identifies selected regions of interest on the maps and calculates the cloudiness situation at a given location. Halcon is the comprehensive standard software for machine vision with an integrated development environment that is used worldwide. Figure 2 summarizes the procedure and the operators used in the developed algorithm to obtain map-based cloudiness factors.

ISSN: 0976 – 2965
IJBET (2017), 6(4):32-37

To analyze the maps, three rectangles were subjectively set as regions of interest (Figure 3). The coordinates in pixels of the rectangles 1, 2 and 3 are (467, 693, 470, 700), (485, 690, 487, 694) and (489, 713, 491, 718), respectively. On the green background of the map, white colour defined clouds intensity and distribution, blue colour represented rain while pink colour indicated presence of snow. Due to presence of these colours on the map, access channel 3 in the algorithm was considered for this analysis.

A linear interpolation method (Eqn. 1) was then used to compute the cloudiness factors for the three regions. This was done using the *gray_features* operator which gives the mean gray value of the selected region. RGB colour images are a combination of the three primary colours red (R), green (G) and blue (B). RGB values are positive and range from 0 to 255. Due to presence of white, blue and pink colours on the map, channel 3 (blue colour) was considered for this analysis. This channel ensured that the presence of rain on the map (intensity of blue colour) was taken into consideration while computing the cloudiness factors. The cloudiness factor C ranges from 0 (clear-sky) to 1 (cloudy).

$$C = C_{min} + \left(\frac{grayval - grayval_{offset}}{grayval_{max} - grayval_{offset}} \right) \cdot (C_{max} - C_{min}) \quad (1)$$

where, C is cloudiness factor, C_{max} is maximum cloudiness factor, C_{min} is minimum cloudiness factor, $grayval$ is gray value of the region at any given time, $grayval_{offset}$ is offset gray value of the green background = 35 and $grayval_{max}$ is maximum possible gray value = 256.

A CNR 4 net radiometer (Delft, The Netherlands) was the main instrument used in the longwave radiation measurement. The CNR 4 design is such that both the upward facing and downward facing instruments measure the energy received from the whole hemisphere. Other than the two pyranometers integrated into the instrument body for measurement of solar radiation, the two pyrgeometers were specifically used for infrared measurement (longwave radiation). Thus, the downwelling and upwelling longwave radiation components are measured independently and it was therefore possible to assess the values simulated with the estimated cloudiness factors. In particular, the downwelling longwave radiation (from sky to the cover surface) was quite important in this study since the simulated value of the same is a function of cloudiness. The longwave radiation measurements using the developed thermal box system were carried out at the Biosystems Engineering Section, Institute of Horticultural Production Systems, Leibniz Universität Hannover (52.39° N, 9.706° E and altitude 52.3 m above mean sea level). This measurement site is located in Lower Saxony, Germany.

2. Application in modelling of longwave radiation

The equation for downwelling longwave radiation LW_d under all-sky conditions has the general form (Eqn. 2) [8, 9, 10]:

$$LWR_d = \varepsilon_{ac} \cdot \left(1 + b \cdot C^d\right) \cdot \sigma \cdot T_a^4 \quad (2)$$

where, ε_{ac} is clear-sky atmospheric emissivity, b and d are coefficients determined experimentally, C is cloudiness factor, σ is Stefan-Boltzmann constant = 5.67×10^{-8} W/(m^{2}K^4), and T_a is air temperature.

According to Howard and Stull [11], longwave radiation from the surrounding objects such as trees can enhance the total downwelling longwave radiation $LW_{d,t}$ and should not be neglected. $LW_{d,t}$ is therefore expressed as (Eqn. 3):

$$LWR_{d,t} = LWR_d + \varepsilon_{gnd} \cdot F_{gnd} \cdot \sigma \cdot T_a^4 \quad (3)$$

where, ε_{gnd} is emissivity of ground objects, F_{gnd} is view factor to the ground = $\sin^2(\beta/2)$. β is surface inclination angle, which in this case is 26.5° for the developed measurement system.

An additional term accounting for the reflected downwelling radiation is incorporated in computation of the upwelling longwave radiation [12]. From the equations above, the sum of the emitted longwave radiation by the surface LWR_u and the reflected downwelling longwave radiation gives the total upwelling longwave radiation $LWR_{u,t}$ [13]. The difference in all upwelling radiation and all downwelling radiation must result in the effective thermal radiation exchange. Thus, for an exterior surface with emissivity ε_s, the $LWR_{u,t}$ is expressed in the form given by (Eqn. 4) [14]:

$$LWR_{u,t} = LWR_u + (1 - \varepsilon_s) \cdot LWR_d \quad (4)$$

ISSN: 0976 – 2965
IJBET (2017), 6(4):32-37

Figure 1. Thermal box for radiation exchange measurement at an exterior surface.

Table 1. Cloudiness prediction approaches considered in this study.

No.	Approach	Frequency	Prediction technique	Source
1	Octas	Once per hour	Manual inspection	[6]
2	Weather maps	Every 5 minutes	Computer-based image analysis	[7]

Table 2. Cloudiness factors derived from sample weather maps and octas.

Weather map	RGB values	C_{maps}	Octas	C_{octas}
	(52, 77, 35)	0	0	0
	(59, 82, 36)	0.005	0	0
	(81, 112, 55)	0.091	1	0.125
	(100, 117, 85)	0.318	2	0.25
	(122, 130, 115)	0.405	3	0.375
	(147, 149, 144)	0.523	4	0.5
	(170, 170, 170)	0.609	5	0.625
	(199, 199, 199)	0.745	6	0.75
	(223, 223, 225)	0.864	7	0.875
	(43, 169, 253)	0.991	8	1
	(255, 194, 254)	0.995	8	1

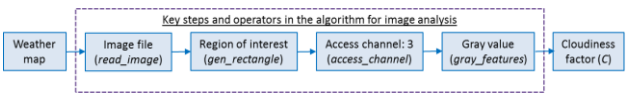

Figure 2. Procedure overview for the image analysis with Halcon 11.0.

Figure 3. A weather map (left) and an exploded view of the region under study (right).

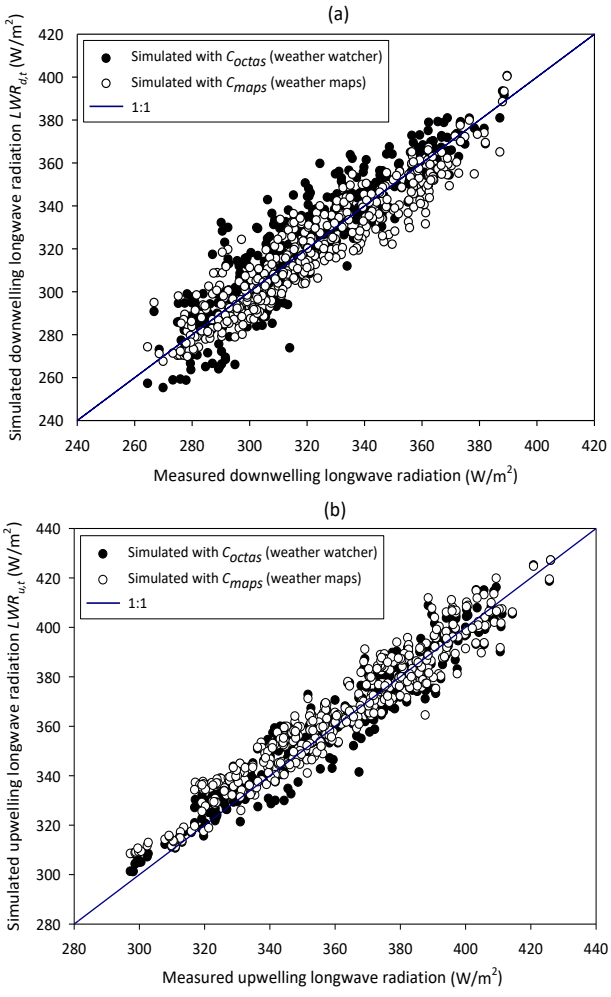

Figure 4. Comparison of simulated and measured nighttime longwave radiation: (a) downwelling (n = 455), and (b) upwelling (n = 455).

ISSN: 0976 – 2965
IJBET (2017), 6(4):32-37

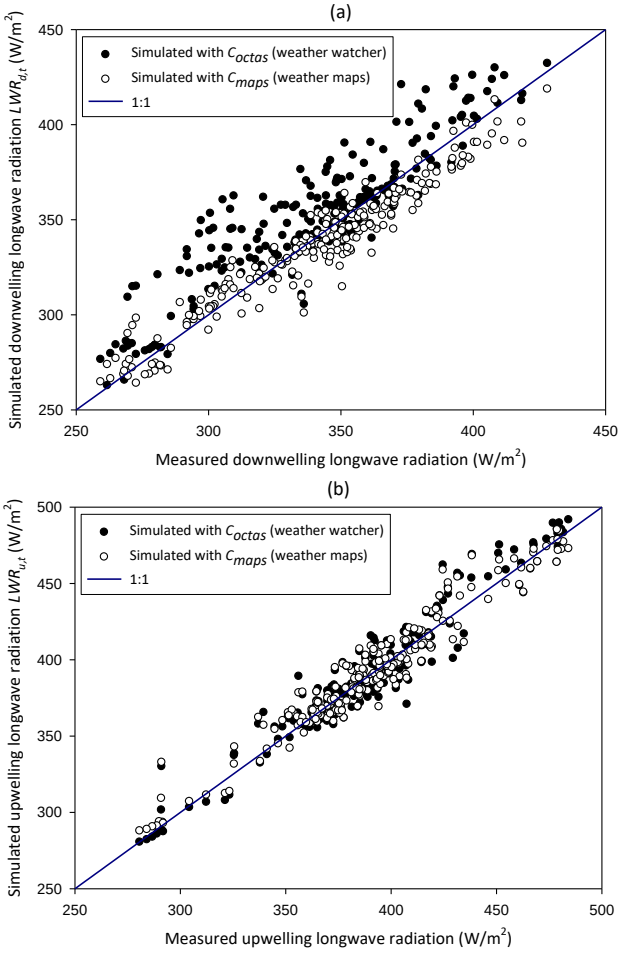

Figure 5. Comparison of simulated and measured daytime longwave radiation: (a) downwelling (*n* = 229), and (b) upwelling (*n* = 229).

RESULTS

The results show that the two cloudiness prediction approaches (weather watchers and weather maps) have similar trends (Table 2). The cloud cover intensity and distribution was well captured in terms of the calculated cloudiness factors C_{octas} (assigned by the weather watcher) and C_{maps} (analyzed weather maps). However, a small statistically significant difference ($p < 0.001$) between the two cloudiness prediction approaches (weather watcher and weather maps) was found. Further comparison indicates that the mean error of cloudiness prediction was higher during the day (0.280) than at night (0.143). This could be attributed to influences by light and solar radiation.

Comparisons between the simulated downwelling longwave radiation ($LWR_{d,t}$) and upwelling longwave radiation ($LWR_{u,t}$) and their corresponding measured longwave radiation fluxes at night are presented in Figure 4. The $LWR_{d,t}$ and $LWR_{u,t}$ values varied in the range of about 255 W/m^2 to 400 W/m^2 and 300 W/m^2 to 430 W/m^2, respectively. Heating of the measurement system at night increased the surface temperatures, thereby increasing the total upwelling longwave radiation $LWR_{u,t}$. Due to the two approaches utilized for cloudiness prediction (the octas assigned by the weather watcher and the analyzed weather maps), simulation was always in two datasets. For both $LWR_{d,t}$ and $LWR_{u,t}$, it is noted that better model prediction was obtained for the nighttime observation period. The map-based simulated data seem to be closer to the 1:1 line than those simulated with octas.

The simulated downwelling longwave radiation $LWR_{d,t}$ and upwelling longwave radiation $LWR_{u,t}$ and the corresponding measured values during the day are compared in Figure 5. Generally, $LWR_{d,t}$ ranged between 260 W/m^2 and 430 W/m^2 while $LWR_{u,t}$ values were in the range of 280 W/m^2 to 490 W/m^2. Despite no heating of the thermal box during daytime, the $LWR_{u,t}$ values were equally high due to solar radiation presence. It is also evident from the figure that simulation with the cloudiness factor derived from octas (assigned by the weather watcher) led to overestimation of $LWR_{d,t}$ during the day. The octa-based $LWR_{d,t}$ values deviated more from the 1:1 line than the map-based ones. However, simulation of $LWR_{u,t}$ with both cloudiness approaches were not significantly different ($p > 0.001$) from each other.

DISCUSSION

The values of coefficient of determination (R^2) for the simulation with cloudiness factors C_{octas} and C_{maps} during the day were 0.818 and 0929, respectively for $LWR_{d,t}$ and 0.924 and 0.935, respectively for $LWR_{u,t}$. Under the nighttime condition, the R^2 values for simulation with C_{octas} and C_{maps} are 0.870 and 0.910, respectively for $LWR_{d,t}$ and 0.912 and 0.924, respectively for $LWR_{u,t}$. The estimated cloudiness factors (C_{octas} from weather watcher and C_{maps} from analyzed weather maps) were necessary for the radiation modelling (see Table 2). These cloudiness factors were then implemented into the effective atmospheric emissivity parameterization. The inclusion of the cloudiness factor in the model parameters provides an appreciable improvement on the simulation [15]. Clouds are known to alter longwave radiative profile through emission of longwave radiation from cloud base [5]. Generally, the presence of clouds increases atmospheric irradiance received at the surface. This could be attributed to the fact that radiation from water vapour and carbon dioxide in the lower atmosphere gets supplemented by emission from clouds in the waveband which the gaseous emission lacks [16]. However, clouds should not be expected to increase sky radiation by more than 40% even under completely overcast conditions

[17]. Cooler clouds, on the other hand, reduce the amount of heat that radiates into space by absorbing the heat radiating from the surface and re-radiating some of it back down. Despite this scenario, this cooling effect of clouds is partly offset by a blanketing effect (reflection of infrared radiation from the underside of clouds).

The longwave radiation heat exchange between surfaces is dependent on their temperatures, spatial relationships between these surfaces and surroundings, and material properties of the surfaces. During the nighttime, the glass-covered greenhouse surface model exchanges longwave radiation with the sky, air and ground. A portion of the energy reaching the surface is reflected skyward where it may again interact with clouds and these radiative interactions constitute the surface cloud radiative forcing over a given area, a factor used to determine the impact of clouds on irradiance [5]. Generally, the presence of cloud increases atmospheric irradiance received at the surface. This could be attributed to the fact that radiation from water vapour and carbon dioxide in the lower atmosphere gets supplemented by emission from clouds in the waveband which the gaseous emission lacks [12].

CONCLUSION

For accurate parameterization of downwelling longwave radiation under all-sky conditions, the cloudiness factor is needed and the two prediction approaches used in this study (octas assigned by weather watcher and analyzed weather maps) gave reliable results. Generally, the map-based cloudiness factors, generated by the computer vision approach, performed best in radiation modelling and they can be used in different modelling applications in agriculture. With the developed thermal box simulating an exterior greenhouse surface and the prevailing atmospheric conditions, the findings demonstrated that prediction models provide a more realistic understanding of thermal radiation exchange mechanisms if cloudiness is used in the simulation. The view factor in the model is a function of surface orientation and is useful in defining the proportion of radiation exchange between the cover surface and the sky. The generated model explains the relationships between specific exterior thermal performance of the cover, atmospheric conditions and energy consumption. Consequently, the radiation models improved with accurate cloudiness factors are useful for efficient greenhouse production throughout the year and the results can be applied to any building surface. In this way, it is possible to further determine the significance of the radiative heat transfer coefficient in the overall heat transfer coefficient.

ACKNOWLEDGEMENT

The author thanks the Biosystems Engineering Section at the Leibniz Universität Hannover, Germany for their support. The joint scholarship support between the National Commission for Science, Technology and Innovation (NACOSTI, Kenya) and the German Academic Exchange Service (DAAD, Germany) provided to the author is also highly acknowledged.

REFERENCES

[1] Van der Veen, S.H. (2013). Improving NWP model cloud forecasts using meteosat second-generation imagery. Monthly Weather Review, 141(5): 1545-1557.

[2] Vukicevic, T., Greenwald, T., Zupanski, M., Zupanski, D., Vonder Haar, T. & Jones, A.S. (2004). Mesoscale cloud state estimation from visible and infrared satellite radiances. Monthly Weather Review, 132(12): 3066-3077.

[3] Flerchinger, G.N., Xaio, W., Marks, D., Sauer, T.J. & Yu, Q. (2009). Comparison of algorithms for incoming atmospheric long-wave radiation. Water Resources Research, 45(W03423): 1-13.

[4] Marty, C. & Philipona, R. (2000). The clear-sky index to separate clear-sky from cloudy-sky situations in climate research. Geophysical Research Letters, 27(17): 2649-2652.

[5] Key, E.L. & Minnett, P.J. (2004). Estimating polynya cloudiness. Gayana (Concepc.) TIProc Concepciòn, 68(2): 311-316.

[6] German Weather Service (Deutscher Wetterdienst, DWD) (2013). Web weather request and distribution system (WebWerdis). http://werdis.www.dwd.de (last accessed July 9, 2013).

[7] Weather Online (WetterOnline) (2013). Weather maps – clouds, rain and snow at a glance. http://www.wetteronline.de (last accessed July 9, 2013).

[8] Choi, M., Jacobs, J.M. & Kustas, W.P. (2008). Assessment of clear and cloudy sky parameterizations for daily downwelling longwave radiation over different land surfaces in Florida, USA. Geophysical Research Letters, 35(L20402): 1-6.

[9] Dos Santos, C.A.C., Da Silva, B.B., Rao, T.V.R., Satyamurty, P. & Manzi, A.O. (2011). Downward longwave radiation estimates for clear-sky conditions over northeast Brazil. Revista Brasileira de Meteorologia, 26(3): 443-450.

[10] Duarte, H.F., Dias, N.L. & Maggiotto, S.R. (2006). Assessing daytime downward longwave radiation estimates for clear and cloudy skies in southern Brazil. Agricultural and Forest Meteorology, 139(3-4): 171-181.

[11] Howard, R. & Stull, R. (2013). Modeling the downwelling longwave radiation over a groomed ski run under clear skies. Journal of Applied Meteorology and Climatology, 52(7): 1540-1553.

[12] Tang, B.H. & Li, Z.L. (2008). Estimation of instantaneous net surface longwave radiation from MODIS cloud-free data. Remote Sensing of Environment, 112(9): 3482-3492.

[13] Liang, S.L. (2004). Quantitative remote sensing of land surfaces. John Wiley & Sons, New Jersey, USA.

[14] Ronoh, E.K. & Rath, T. (2015). Modelling of longwave radiation exchange at greenhouse surfaces under all-sky conditions. Agricultural Engineering International: CIGR Journal, 17(4): 23-35.

[15] Ronoh, E.K. & Rath, T. (2014). Investigations on the external thermal radiation exchanges between the glass-covered greenhouse surfaces and the sky. DGG-Proceedings, 4(6): 1-5.

[16] Iziomon, M.G., Mayer, H. & Matzarakis, A. (2003). Downward atmospheric longwave irradiance under clear and cloudy skies: measurement and parameterization. Journal of Atmospheric and Solar-Terrestrial Physics, 65(10): 1107-1116.

[17] Kimball, B.A., Idso, S.B. & Aase, J.K. (1982). A model of thermal radiation from cloudy and overcast skies. Water Resources Research, 18(4): 931-936.